https://doi.org/10.5194/gmd-2021-346
Preprint. Discussion started: 22 November 2021


Geoscientific Model Development
Discussions
Open Access

# Embedding a One-column Ocean Model (SIT 1.06) in the Community Atmosphere Model 5.3 (CAM5.3; CAM5–SIT v1.0) to Improve Madden–Julian Oscillation Simulation in Boreal Winter

Yung-Yao Lan, Huang-Hsiung Hsu, Wan-Ling Tseng, and Li-Chiang Jiang

Research Center for Environmental Changes, Academia Sinica, Taipei 11529, Taiwan

*Correspondence to*: Yung-Yao Lan (yylan887@gmail.com)

https://doi.org/10.5194/gmd-2021-346
Preprint. Discussion started: 22 November 2021

Geoscientific Model Development
Discussions
Open Access

**Abstract**

The effect of the air–sea interaction on the Madden–Julian Oscillation (MJO) was investigated using the one-column ocean model Snow–Ice–Thermocline (SIT 1.06) embedded in the Community Atmosphere Model 5.3 (CAM5.3; hereafter CAM5–SIT v1.0). The SIT model with 41 vertical layers was developed to simulate sea surface temperature (SST) and upper-ocean temperature variations with a high vertical resolution that resolves the cool skin and diurnal warm layer and the upper oceanic mixed layer. A series of 30-year sensitivity experiments were conducted in which various model configurations (e.g., coupled versus uncoupled, vertical resolution and depth of the SIT model, coupling domains, and absence of the diurnal cycle) were considered to evaluate the effect of air–sea coupling on MJO simulation. Most of the CAM5–SIT experiments exhibited higher fidelity than the CAM5-alone experiment in characterizing the basic features of the MJO such as spatiotemporal variability and the eastward propagation in boreal winter. The overall MJO simulation performance of CAM5–SIT benefited from (1) better resolving the fine structure of upper-ocean temperature and therefore the air–sea interaction that resulted in more realistic intraseasonal variability in both SST and atmospheric circulation and (2) the adequate thickness and vertical resolution of the oceanic mixed layer. The sensitivity experiments demonstrated the necessity of coupling the tropical eastern Pacific in addition to the tropical Indian Ocean and the tropical western Pacific. Enhanced MJO could be obtained without considering the diurnal cycle in coupling.

https://doi.org/10.5194/gmd-2021-346
Preprint. Discussion started: 22 November 2021



## 1. Introduction

The Madden–Julian Oscillation (MJO) is a tropical large-scale convection circulation system that propagates eastward across the warm pool region from the tropical Indian Ocean (IO) to the western Pacific (WP) on an intraseasonal time scale (Madden and Julian, 1972). The MJO is not just an atmospheric phenomenon. The findings of the multination joint field campaign called the Cooperative Indian Ocean Experiment on Intraseasonal Variability in the Year 2011/Dynamics of the MJO (de Szoeke et al., 2017; Johnson and Ciesielski, 2017; Pujiana et al., 2018; Yoneyama et al., 2013; Zhang and Yoneyama, 2017) revealed vigorous air–sea coupling during the evolution of the MJO (Chang et al., 2019; DeMott et al., 2015; Jiang et al., 2015, 2020; Kim et al., 2010; Li et al., 2016; Li et al., 2020; Newman et al., 2009; Pei et al., 2018; Tseng et al., 2014). During the suppression of convection, the MJO propagates eastward with light winds, which is accompanied by enhanced downwelling shortwave radiation absorption, weaker upward latent and sensible fluxes, less cloudiness and precipitation, and weaker vertical mixing in the upper ocean, thus causing an increase in the upper-ocean temperature. In the following active phase when deep convection occurs, downwelling shortwave radiation is reduced and stronger westerly winds enhance evaporation and sensible heat loss from the ocean surface, thus causing a decrease in the upper-ocean temperature (DeMott et al., 2015; Madden and Julian, 1972, 1994; Zhang, 2005).

In addition to the ocean surface, the structure of the upper ocean also evolves. Alappattu et al. (2017) reported that during an MJO event, surface flux perturbations cause changes in the ocean thermohaline structure, thus affecting the mixed-layer temperature. The following change in sea surface temperature (SST) can further affect atmospheric circulation of the MJO. Variations in SST mediate heat exchange across the air–sea interface. Although SST responds to atmospheric forcing, its modulation

https://doi.org/10.5194/gmd-2021-346
Preprint. Discussion started: 22 November 2021



of surface heat fluxes provides feedback to the atmosphere (DeMott et al., 2015; Jiang et al., 2020). Li et al. (2008, 2020) proposed that the phase relationship between SST and convection implies a delayed air–sea interaction mechanism whereby a preceding active-phase MJO may trigger an inactive-phase MJO through the delayed effect of the induced SST anomaly over the IO. The reduction in SST caused by a preceding active-phase MJO may, in turn, yield delayed ocean feedback that initiates a suppressed-phase MJO, and vice versa. The nonnegligible effect of intraseasonal SST variations caused by surface fluxes suggests that the ocean state can affect the MJO (DeMott et al., 2015, 2019; Hong et al., 2017; Li et al., 2020).

Since its discovery almost five decades ago, the MJO remains a phenomenon that poses a challenge to the capacity of state-of-the-art atmospheric general circulation models (AGCMs) and climate models such as those participating in the Coupled Model Intercomparison Project phase 5 and 6 to generate successful simulations (Ahn et al., 2017, 2020; Bui and Maloney 2018; Jiang et al., 2020; Hung et al., 2013; Kim et al., 2011).

Recent studies have reported that air–sea coupling improves the representation of the MJO in numerical simulation (Bernie et al., 2008; Crueger et al., 2013; DeMott et al., 2015; Li et al., 2016; Li et al., 2020; Tseng et al., 2014; Woolnough et al., 2007). Tseng et al. (2014) indicated that effectively resolving the upper-ocean warm layer to capture temperature variations in the upper few meters of the ocean could improve MJO simulation. DeMott et al. (2015) suggested that the tropical atmosphere–ocean interaction may sustain or amplify the pattern of the enhanced and suppressed atmospheric convection of the eastward propagation. DeMott et al. (2019) demonstrated that the improved MJO eastward propagation in four coupled models resulted from enhanced low-level convective moistening for a rainfall rate of >5 mm day$^{-1}$ due to air–sea coupling. In addition, numerical experiments have been

https://doi.org/10.5194/gmd-2021-346
Preprint. Discussion started: 22 November 2021



performed to investigate the effect of the diurnal cycle on the MJO (Hagos et al., 2016; Oh et al., 2013), with the results suggesting that the strength and propagation of the MJO through the Maritime Continent (MC) were enhanced when the diurnal cycle was ignored.

Although previous studies have demonstrated the importance of considering the air–sea interaction in a numerical model to improve MJO simulation, additional details regarding model configuration (e.g., vertical resolution, depth of the ocean mixed layer, coupling domain, and absence of the diurnal cycle) have not been systematically explored. Tseng et al. (2014) coupled the one-column ocean model Snow–Ice–Thermocline (SIT; Tu and Tsuang, 2005) to the fifth generation of the ECHAM AGCM (ECHAM5–SIT) and indicated that a vertical resolution of 1 m was essential to yield an improved simulation of the MJO with a realistic strength and eastward propagation speed.

In this study, we coupled the SIT model to the Community Atmosphere Model version 5.3 (CAM5.3; Neale et al., 2012)—the atmosphere component of the Community Earth System Model version 1.2.2 (CESM1.2.2; Hurrell et al., 2013)—to explore how the air–sea interaction in AGCMs can improve MJO simulation. The CAM5.3, which has been widely used for the long-term simulation of the climate system, could not efficiently simulate the eastward propagation of the MJO; instead, the model simulated a tendency for the MJO to move westward in the IO (Boyle et al., 2015, Jiang et al, 2015). By contrast, the updated CESM2 with the new CAM6 could realistically simulate the MJO (Ahn et al., 2020; Danabasoglu et al., 2020). Thus, the well-explored CAM5, which does not produce a realistic MJO, appears to be a favorable choice for exploring how coupling a simple one-dimensional (1-D) ocean model, such as the SIT model, can improve MJO simulation, as well as the effects of model configuration. Such a study can also enhance our understanding

https://doi.org/10.5194/gmd-2021-346
Preprint. Discussion started: 22 November 2021



regarding the air–sea coupling's effect on the MJO.

This study examined how air–sea coupling can improve MJO simulation, especially that of the eastward propagation that has been poorly simulated in many climate models. The MJO that exhibits a more substantial eastward propagation in boreal winter than in other seasons was the targeted feature in this study. We conducted a series of 30-year numerical experiments by considering various model configurations (e.g., coupled versus uncoupled, vertical resolution and depth of the SIT model, coupling domains, and absence of the diurnal cycle) to investigate the effect of air–sea coupling. This paper is organized as follows. Section 2 describes the data, methodology, and model setup. Section 3 presents the design of coupled model experiments. Section 4 describes the effect of various model configurations on the MJO simulation determined through detailed MJO diagnostics. A discussion and conclusions are provided in Section 5.

## 2. Data, methodology, and model description

### 2.1 Observational data and analysis methods

The data analyzed in this study include precipitation from the Global Precipitation Climatology Project, outgoing longwave radiation (OLR) and daily SST (Optimum Interpolation SST) from the National Oceanic and Atmosphere Administration (NOAA), and parameters from the ERA-Interim reanalysis (Adler et al., 2003; Dee et al., 2011; Lee et al., 2011; Reynolds and Smith, 1995; Schreck et al., 2018). The initial SST data for the SIT model were obtained from the Hadley Centre Sea Ice and Sea Surface Temperature dataset (Rayner et al., 2003) and the ocean subsurface data (40-layer climatological ocean temperature, salinity, and currents) for nudging were retrieved from the National Centers for Environmental Prediction (NCEP) Global Ocean Data Assimilation System (GODAS; Behringer and Xue,

https://doi.org/10.5194/gmd-2021-346
Preprint. Discussion started: 22 November 2021



2004). Ocean bathymetry was derived from the NOAA ETOPO1 data (Amante and Eakins, 2009) and interpolated into 1.9° × 2.5° horizontal resolution.

We used the CLIVAR MJO Working Group diagnostics package (CLIVAR, 2009) and a 20–100-day filter (Kaylor, 1977; Wang et al., 2014) to determine intraseasonal variability. MJO phases were defined following the index (namely, RMM1 and RMM2) proposed by Wheeler and Hendon (2004), which considers the first two principal components of the combined near-equatorial OLR and zonal winds at 850 and 200 hPa. The band-passed filtered data were used for calculating the index and defining phases.

## 2.2 Model description

### 2.2.1 CAM5.3

The CAM5.3 used in this study has a horizontal resolution of 1.9° latitude × 2.5° longitude and 30 vertical levels with the model top at 0.1 hPa. The MJO could not be realistically simulated in the CAM5.3. Boyle et al. (2015) demonstrated that although making the deep convection dependent on SST improved the simulation of the MJO variance, it exerted a significant negative effect on the mean-state climate of low-level cloud and absorbed shortwave radiation. By comparing the simulation results of an uncoupled and coupled CAM5.3, Li et al. (2016) suggested that air–sea coupling and the convection scheme most significantly affected the MJO simulation in the climate model.

### 2.2.2 1-D high-resolution TKE ocean model

The 1-D high-resolution turbulence kinetic energy ocean model SIT was used to simulate the diurnal fluctuation of SST and surface energy fluxes. The model was well verified against surface and subsurface observations in the South China Sea (Lan et

https://doi.org/10.5194/gmd-2021-346
Preprint. Discussion started: 22 November 2021



al., 2010) and the tropical WP (Tu and Tsuang, 2005). Variations in sea water temperature ($T$), current ($\vec{u}$), and salinity ($S$) were determined (Gaspar et al., 1990) using the following equations.

$$\frac{\partial T}{\partial t} = (k_h + v_h)\frac{\partial^2 T}{\partial z^2} + \frac{R_{sn}}{\rho_{w0} c_w}\frac{\partial F}{\partial z} \quad (1)$$

$$\frac{\partial \vec{u}}{\partial t} = -f\,\hat{k} \times \vec{u} + (k_m + v_m)\frac{\partial^2 \vec{u}}{\partial z^2} \quad (2)$$

$$\frac{\partial S}{\partial t} = (k_h + v_h)\frac{\partial^2 S}{\partial z^2} \quad (3)$$

where $R_{sn}$ is the net solar radiation at the surface (W m$^{-2}$), $F(z)$ is the fraction (dimensionless) of $R_{sn}$ that penetrates to the depth $z$, and $k_h$ and $k_m$ are eddy diffusion coefficients for heat and momentum (m$^2$ s$^{-1}$), respectively. The value of $k_h$ within the cool skin layer and that of $k_m$ within the viscous layer were set to zero. Molecular transport is the only mechanism for the vertical diffusion of heat and momentum in the cool skin and viscous layer, respectively (Hasse, 1971; Grassl, 1976; Wu, 1985).The parameters $\nu_m$ and $\nu_h$ are the molecular diffusion coefficients for momentum and temperature, respectively, $\rho_{w0}$ is the density (kg m$^{-3}$) of water, and $c_w$ is the specific heat capacity at constant pressure (J kg$^{-1}$ K$^{-1}$). $S$ is salinity (‰), $\vec{u}$ is the current velocity (m s$^{-1}$), $f$ is the Coriolis parameter (dimensionless), and $\hat{k}$ is the vertical unit vector (m s$^{-1}$).

The eddy diffusivity for momentum $k_m$ is simulated using an eddy kinetic energy approach based on the Prandtl–Kolmogorov hypothesis as follows:

$$k_m = c_k l_k \sqrt{E} \quad (3)$$

where $c_k = 0.1$ (Gaspar et al., 1990), $l_k$ is the mixing length (m), and $E = 0.5\left(u'^2 + v'^2 + w'^2\right)$ is turbulent kinetic energy. The turbulent kinetic energy ($E$) is determined using a 1-D equation (Mellor and Yamada, 1982) as follows:

https://doi.org/10.5194/gmd-2021-346
Preprint. Discussion started: 22 November 2021

Geoscientific Model Development Discussions
Open Access

$$\frac{\partial E}{\partial t} = \frac{\partial}{\partial z} k_m \frac{\partial E}{\partial z} + k_m \left(\frac{\partial \vec{u}}{\partial z}\right)^2 + k_h \frac{g}{\rho_w} \frac{\partial \rho_w}{\partial z} - c_\varepsilon \frac{E^{3/2}}{l_\varepsilon} \tag{4}$$

where $c_\varepsilon = 0.7$ (Gaspar et al., 1990), $g$ is the gravity (m s$^{-2}$), $\rho_w$ is the density of water (kg m$^{-3}$), and $l_\varepsilon$ is the characteristic dissipation length (m). The mixing length ($l_k$) and dissipation length ($l_\varepsilon$) were determined following the approach reported by Gaspar et al. (1990). This approach is valid for determining the eddy diffusivity of both the ocean mixed layer and surface layer.

In the SIT model setting, the specific heat of sea water is a constant (4186.84 J kg$^{-1}$ K$^{-1}$), and the Prandtl number in water is defined as the ratio of momentum diffusivity to thermal diffusivity, which is a dimensionless number set as a constant (1.0). The kinematic viscosity is a constant ($1.14 \times 10^{-6}$ m$^2$ s$^{-1}$; Paulson and Simpson, 1981), and the downward solar radiative flux into water with nine wavelength bands was determined following the approach reported by Paulson and Simpson (1981). The minimum turbulent kinetic energy is set to $10^{-6}$ m$^2$ s$^{-2}$, and the zero displacement is set to 0.03 m.

The SIT model determines the vertical profiles of the temperature and momentum of a water column from the surface down to the seabed. To account for the neglected horizontal advection heat flux, the ocean is weakly nudged (by using a 30-day time scale) between 10 and 100 m and strongly nudged (by using a 1-day time scale) below 100 m according to the NCEP GODAS climatological ocean temperature; no nudging is performed for depths under 10 m. Considerably fine 41-layer vertical discretization is applied, with 12 layers in the upper 10 m. The resolution in the upper 10 m is considerably fine to capture the upper-ocean warm layer, and the thickness of the first layer below sea surface is 0.05 mm to reproduce the ocean surface cool skin. The 41 levels are at the surface and at the depths of 0.05

https://doi.org/10.5194/gmd-2021-346
Preprint. Discussion started: 22 November 2021



mm, 1.0 cm, 2.0 cm, 3.0 cm, 4.0 cm, 5.0 cm, 6.0 cm, 7.0 cm, 8.0 cm, 9.0 cm, 10.0 cm, 16.8 cm, 29.5 cm, 43.6 cm, 59.2 cm, 76.9 cm, 96.8 m, 119.4 cm, 145.3 cm, 174.9 cm, 208.9 m, 248.3 cm, 293.8 cm, 346.8 cm, 408.4 cm, 480.2 cm, 564.3 cm, 662.6 cm, 777.9 cm, 913.1 cm, 1072.0 cm, 1258.8 cm, 1478.6 cm, 1737.3 cm, 2042.0 cm, 2401.1 cm, 2824.4 cm, 3323.6 cm, 3912.4 cm, and 4607.1 cm. The SIT model calculates data two times for each CAM5 time step (30 min; i.e., coupling 48 times per day).

## 3. Experimental setup

Five sets of 30-year numerical experiments (Table 1) were conducted to investigate the effect of the air–sea interaction on the MJO simulation. In all simulations, the CAM5.3 was forced by observed climatological monthly SST except in the coupling region where the SIT model determined the upper ocean temperature. The five experiment sets were (1) a standalone CAM5.3 simulation forced by observed climatological monthly SST (A–CTL) and a coupled CAM5–SIT v1.0 simulation (C–30NS; 41 vertical levels, coupling in the entire tropics between 30°S and 30°N with a diurnal cycle); (2) an upper-ocean vertical resolution experiment (C–LR12m and C–LR34m): two coarse vertical resolution simulations with a thickness of 11.8 and 34.2 m, respectively, at the third layer; (3) a lower ocean boundary experiment: three simulations with the lower boundary of the SIT model at 10 m (C–HR1mB10m), 30 m (C–HR1mB30m), and 60 m (C–HR1mB60m)]; (4) a regional coupling experiment: simulations with four coupling domains, namely the latitudinal effect [0°N–30°N (C–0_30N) and 0°S–30°S (C–0_30S)] and the longitudinal effect [30°E–180°E (C–30_180E) and 30°E–75°W (C–30E_75W)] (see the coupling domain in Fig. 1); and (5) a diurnal coupling experiment: a nondiurnal simulation that

https://doi.org/10.5194/gmd-2021-346
Preprint. Discussion started: 22 November 2021



considers the air–sea interaction by calculating ocean surface fluxes based on daily mean atmospheric variables and SST (C–30NS–nD), with the coupling frequency maintained 48 times per day to prevent the local time in different regions from being inconsistent when coupling once a day. Greenhouse gas concentrations were fixed at the values observed in the year 2000.

The main codes of the SIT model in Fortran 90 are packaging in independent and original subprograms, with data and interface blocks in modules, that creates explicit interfaces between the CAM5.3 and the SIT model without a coupler. In addition, these modules contain dynamically allocable arrays and the independent I/O procedures of the SIT model. The coupler in the CAM5–SIT only brokers communication interchanges between the simulated SST and calculated oceanic surface fluxes.

## 4. Results and Discussion

The realistic simulation of the MJO has always been a major bottleneck in the development of climate models. In this section, we demonstrate how air–sea coupling using a 1-D ocean mixed-layer model significantly improves the MJO simulation by the CAM5.3. The period between November and April when the MJO is the most prominent was the targeted season in this study.

### 4.1 Improvement of MJO simulation through air–sea coupling

This subsection compares the MJO simulation of the coupled model (C–30NS) with that of the uncoupled AGCM (A–CTL) forced by climatological monthly SST to demonstrate the effect of air–sea coupling on the MJO simulation by coupling the SIT model to the CAM5.3 in the tropical belt (30°N–30°S).

https://doi.org/10.5194/gmd-2021-346
Preprint. Discussion started: 22 November 2021


Geoscientific Model Development Discussions
Open Access

#### 4.1.1 Wavenumber–frequency spectra and eastward propagation characteristics

A wavenumber–frequency spectrum (W–FS) analysis was conducted to quantify propagation characteristics simulated in different experiments. The spectra of unfiltered U850 in observation, C–30NS, and A–CTL are shown in Fig. 2a–c, respectively. The coupled C–30NS effectively simulated the observed eastward-propagating signals at zonal wavenumber 1 and 30–80-day periods (Fig. 2a–b), although with a slightly larger amplitude. By contrast, the uncoupled A–CTL did not effectively simulate the observed characteristics; instead, it simulated both eastward (wavenumber 1)- and westward (wavenumber 2)-propagating signals with an unrealistic spectral shift to time scales longer than the observed 30–80-day period.

The major features of the simulated MJO propagation were examined. Figure 2d–f show the time evolution of intraseasonal precipitation and U850 anomalies in Hovmöller diagrams; specifically, lagged correlation coefficients between precipitation at 10°S–5°N, 75–100°E with the average precipitation at 10°N–10°S and U850 anomalies along the equator. Figure 2d indicates eastward propagation for both precipitation and U850 from the eastern IO to the dateline, with precipitation leading U850 by approximately a quarter of a cycle. The Hovmöller diagram derived from the C–30NS (Fig. 2e) exhibits the key characteristics of eastward propagation for both precipitation and U850 and the relative phases between the two, although the simulated correlation was slightly weaker than that observed. By contrast, the uncoupled A–CTL simulated intraseasonal signals that propagated westward over the IO and simulated weak and much slower eastward propagation crossing the MC and WP (Fig. 2f). The contrast between Fig. 2e and 2f demonstrated that coupling a 1-D ocean TKE ocean model alone could lead to a significant improvement in an AGCM in simulating the major characteristics (e.g., amplitude, propagation direction and

https://doi.org/10.5194/gmd-2021-346
Preprint. Discussion started: 22 November 2021



speed, and phase relationship between precipitation and circulation) of the MJO.

### 4.1.2 Coherence of the simulated MJO

Cross-spectral analysis was performed to examine coherence and phase lag between tropical circulation and convection, which were plotted over the tropical wave spectra. Figure 2g–i show the symmetric part (e.g., Wheeler and Kiladis, 1999) of OLR and U850 in observation, C–30NS, and A–CTL, respectively. We present only a magnified display of spectra between the frequency of 0 to 0.35 day$^{-1}$ to highlight the MJO and equatorial Kelvin waves. The most prominent characteristic observed was the peak coherence at wavenumbers 1–3 and a phase lag of approximately 90° in the 30–80-day band for the symmetric component associated with the MJO (Ren et al., 2019; Wheeler and Kiladis 1999). C–30NS simulated strong coherence in this low-frequency band (wavenumber 1) and exhibited a realistic phase lag relationship between U850 and OLR perturbations. However, the coherence at wavenumbers 2–3 for the 30–80-day period simulated by C–30NS was weaker than that observed. In addition, this undersimulation was noted in CCSM4 (Subramanian et al., 2011), the uncoupled and coupled CAM4 and CAM5 (Li et al., 2016), and NorESM1-M (Bentsen et al., 2013), which had a version of the CAM as an AGCM. In summary, C–30NS produced coherent and energetic patterns in the eastward-propagating intraseasonal fluctuations of U850 and OLR in the tropical IO and WP that are generally consistent with the MJO characteristics. By contrast, the MJO characteristics in A–CTL were considerably weaker than those in C–30NS and that observed.

### 4.1.3 Horizontal and vertical structures of the MJO across the MC

Figure 2j–o show the horizontal and vertical structures of the MJO when deep convection is the strongest over the MC (i.e., phase 5). Figure 2j–l present the 20–100-day filtered OLR (W m$^{-2}$, shaded) and 850-hPa wind (m s$^{-1}$, vector). C–30NS realistically simulated the enhanced tropical convection over the eastern IO and the Kelvin-wave-like easterly anomalies over the tropical WP despite undersimulating the convection over the MC (Fig. 2j and 2k). By contrast, A–CTL failed to simulate the enhanced convection over the eastern IO and MC; instead, it simulated considerably weaker convection and easterly winds over the MC and WP, respectively, than that observed (Fig. 2j and 2l).

Figure 2m–o show the vertical–longitudinal profiles of 20–100-day filtered 15°N–15°S averaged vertical velocity (OMEGA; Pa s$^{-1}$, shaded) and moist static energy (MSE) anomalies (W m$^{-2}$, contour) at phase 5. The spatial distribution of negative OMEGA (ascending motion) anomalies generally agreed with OLR anomalies in C–30NS simulation and observation over the Indo-Pacific region (Fig. 2m and 2n). The observed relative spatial relationship between the ascending motion and MSE was well simulated in C–30NS. For example, positive MSE anomalies on the eastern side of the anomalous ascent demonstrated that the energy recharge process occurs in advance of the MJO convection over the lower-tropospheric easterlies (Fig. 2j and 2k), whereas negative MSE anomalies on the western side revealed that the discharge process occurs during and after convection over the lower-tropospheric westerlies. By contrast, this phase relationship, considered to be an essential feature leading to the eastward propagation of an MJO (Hannah and Maloney 2014; Heath et al., 2021), was not properly simulated in A–CTL (Fig. 2o), in which the simulated weak negative OMEGA was located between negative and positive MSE anomalies over weak lower-tropospheric wind anomalies and associated with weak convection over the MC (Fig. 2l).

The observed temporal evolution (Fig. 3a) indicated that convection originating

https://doi.org/10.5194/gmd-2021-346
Preprint. Discussion started: 22 November 2021



in the western IO was enhanced during its eastward propagation to the MC where it reached the peak amplitude and then gradually weakened when continuing moving eastward to the dateline. In C–30NS, this evolution of convectively coupled circulation was realistically simulated, although it was weaker than the observed strength (Fig. 3b). Moreover, the split of convection into two cells off the equator in phase 6 was appropriately simulated in C–30NS (P6 in Fig. 3a and 3b). This split was caused by the topographic and land–sea contrast effects of the MC (Tseng et al., 2017). Associated with the split was the southward detouring of the anomalous convection during the passage of the MJO through the MC (Kim et al. 2017, Tseng et al., 2017; Wu and Hsu, 2009). After the passage of the MJO through the MC, the anomalous convection stayed south of the equator and continued moving eastward to the dateline. In the uncoupled A–CTL, the systematic eastward propagation of convectively coupled MJO circulation from the IO into the MC was not simulated. Instead, the convection over the MC developed in situ at a later stage than that observed (e.g., P6 in Fig. 3c) and dissipated rapidly. The A–CTL simulated a pair of off-equator convection anomalies in the eastern IO during phase 2 (P2 in Fig. 3c) that moved westward toward the central IO and were amplified at later stages (e.g., P4 in Fig. 3c). This unrealistic evolution explains the westward propagation tendency observed in the Hovmöller diagram (Fig. 2f).

#### 4.1.4 Characteristics of air–sea interaction

Figure 4a–c show the longitude–phase diagram in which the 20–100-day filtered precipitation (shaded) and SST (contour) anomalies were averaged over 10°S–10°N to determine the relationship between precipitation and SST fluctuations and to establish a link between air–sea coupling and convection. The propagation of the enhanced convection with positive SST anomalies to the east could be clearly seen in

https://doi.org/10.5194/gmd-2021-346
Preprint. Discussion started: 22 November 2021

Geoscientific Model Development Discussions
Open Access
EGU

observation and C–30NS (Fig. 4a and 4b). The highest SST anomaly (SSTA) led the maximum precipitation anomaly by approximately 2–3 phases, and the SSTA began to decrease following the onset of enhanced precipitation. The observation revealed the following relationship between surface flux and SST: the decreased (increased) latent/sensible heat fluxes and increased (decreased) downward radiation flux leading (lagging) the positive (negative) SSTA east (west) of anomalous deep convection. This well-known lead–lag relationship reflecting the active air–sea interaction in an MJO was realistically simulated in C–30NS (not shown).

The contrast between C–30NS and A–CTL confirms the key role of the air–sea interaction in contributing to the eastward propagation and demonstrates that the eastward propagation simulation can be markedly improved by incorporating the air–sea interaction process in the model, even when using a simple 1-D ocean model such as SIT.

#### 4.1.5 Vertically tilting structure

The warm SST was the key forcing that contributed to the boundary layer convergence before the onset of deep convection (Li et al., 2020; Tseng et al., 2014). Hence, the warmer upper ocean enhances the low-level atmospheric convergence and then leads to enhanced low-level moisture and preconditioned deep convection and eastward propagation. This moistening process associated with warm ocean surface temperature was well simulated in C–30NS but is not shown here. Instead, we present the coupling of moisture divergence (MD) and circulation.

MD and zonal wind anomalies from the surface to the upper troposphere averaged over the 10°S–10°N and 120–150°E region are shown in Fig. 4d–f to depict the relationship between the vertically tilting structure of MD and zonal wind anomalies. Note that the active convection occurred around phase 5. The coupled

https://doi.org/10.5194/gmd-2021-346
Preprint. Discussion started: 22 November 2021



experiment C–30NS (Fig. 4e) realistically simulated the observed deepening of coupled MD and zonal wind anomalies with time (Fig. 4d). An evolution from the right to left seen in each panel of Fig. 4d–f was equivalent to the eastward movement of vertically tilting circulation from the eastern IO into the MC because of the eastward-propagating nature of the MJO. Figure 4d and 4e show that in both observation and C–30NS, the near-surface convergence (negative MD) occurring in the easterly anomalies led the convection and continued deepening up to 500 hPa from phase 2 to phase 6 when the easterly anomalies switched to westerly anomalies. By contrast, this observed evolution of coupled MD–zonal wind anomalies were not appropriately simulated in the uncoupled experiment (Fig. 4f). For example, a slow deepening with time was observed in the MD anomaly but not in the zonal wind anomaly that exhibited a vertically decayed structure, suggesting that MD and wind anomalies were not well coupled, as noted in observation and the coupled experiment.

In observation, the negative near-surface MD anomalies appeared first under the easterly anomaly and continued deepening between the easterly and westerly anomalies. This development in the phase relationship between MD and zonal wind anomalies in both observation and coupled simulation is consistent with the well-known structure embedded in the MJO, namely the near-surface convergence in the easterly phase (i.e., a boundary-layer moistening process; Kiranmayi and Maloney 2011; Li et al., 2020; Tseng et al., 2014), followed by the deep convection when transitioning to the westerly phase. This close phase relationship that is key to the eastward propagation was appropriately simulated in the coupled experiment but not in the uncoupled experiment.

#### 4.1.6 Intraseasonal variance of precipitation

https://doi.org/10.5194/gmd-2021-346
Preprint. Discussion started: 22 November 2021


Figure 4g–i present the spatial distribution of intraseasonal variance of precipitation. In observation, the maximum variance was noted over the tropical eastern IO, MC, and tropical WP. The maximum variance south of the island in the MC and the equator in the tropical WP reflects the southward shift of the MJO deep convection when passing through the MC, partly due to the blocking effect of mountainous islands and the higher moisture content over high SST south of the equator in the region during boreal winter (Kim et al., 2017; Ling et al., 2019; Sobel et al., 2008; Tseng et al., 2017; Wu and Hsu, 2009). Although the coupled experiment failed to simulate the variance maximum in the tropical eastern IO, it appropriately simulated the maximum variance over the tropical WP, reflecting its ability to simulate the eastward propagation of the MJO through the MC. By contrast, the uncoupled A–CTL experiment simulated considerably weaker intraseasonal variance in both the tropical eastern IO and the tropical WP. Figure 4j–l are the 20–100-day filtered SST (K, shaded) and 850-hPa wind (m $s^{-1}$, vector) during MJO phase 7 when deep convection is the strongest over the dateline. The C–30NS realistically simulated the negative SST anomaly over the MC and WP when enhanced tropical convection passed through the MC to the dateline, indicating the capability of the SIT model to reproduce the observed SST anomaly by exchanging surface fluxes between the atmosphere and ocean. In A-CTL, no SST anomaly was evident because the model was forced by prescribed climatological SST. The contrast seen in Fig. 4j–l demonstrates the essential role of atmosphere–ocean coupling in shaping the MJO. A delayed air–sea interaction mechanism was noted, where a preceding active-phase MJO may trigger an inactive-phase MJO through the delayed effect of the induced SST anomaly. In addition, the westerly winds at 850 hPa moving southward between MC and WP were captured by C–30NS and were similar to the observed winds (Fig. 4j and 4k). By contrast, A–CTL forced by climatological monthly SST

(<0.05 K phase$^{-1}$ anomaly) failed to simulate the southward westerly wind of the region extending from the MC to the dateline (Fig. 4l).

**4.2 Effect of upper-ocean vertical resolution**

In the coupled C–30NS, the vertical resolution in the upper 10 m was 1 m. Tseng et al. (2014) suggested that fine vertical resolution is crucial for appropriately simulating the eastward propagation. To investigate the effect of vertical resolution, two coarse-resolution experiments were conducted, which involved increasing the thickness of the first ocean layer (under the cool skin layer) to 11.8 m (C–LR12m) and 34.2 m (C–LR34m), respectively. The W–FS spectral peaks of U850 in C–LR12m were concentrated in eastward-propagating wavenumber 1 at three timescales (e.g., longer than 80 days, 30–80 days, and approximately 30 days; Fig. 5a). In C–LR34m, both eastward and westward signals were simulated with the dominant W–FS timescale that was longer than 80 days (Fig. 5b). The appearance of both eastward and westward signals at a lower frequency implied a stronger stationary tendency or weaker eastward-propagating tendency. This result is consistent with that reported by Tseng et al. (2014) that the coarser the resolution is, the slower is the eastward propagation of the MJO.

The effect of vertical resolution on the MJO simulation can be seen in the Hovmöller diagram. The eastward propagation simulated in C–LR12m (Fig. 5c) markedly weakened after crossing the MC compared with that simulated in C–30NS. In C–LR34m, the quasi-stationary fluctuation and westward propagation were simulated over the IO (Fig. 5d), appearing similar to those in A–CTL. The observed lead–lag relationship between precipitation (zonal wind) and SST was poorly simulated in C–LR12m (Fig. 5e) and even more poorly simulated in C–LR34m (Fig. 5f). This result confirms the finding reported by Tseng et al. (2014) that a higher

https://doi.org/10.5194/gmd-2021-346
Preprint. Discussion started: 22 November 2021



vertical resolution in the first few meters allows for a faster air–sea interaction, thus resulting in a more realistic simulation of the MJO.

### 4.3 Effect of the lowest boundary of the SIT model

The ocean is a vital energy source for the MJO. Although vertical resolution is crucial for the efficiency of air–sea interaction, the thickness of the upper ocean that interacts with the atmosphere represents the heat content to substantiate the MJO. A key question is how thick an oceanic mixed layer should be for a realistic simulation. To explore this issue, three experiments with a model ocean with a 1-m vertical resolution and the ocean bottom at 10, 30, and 60 m, which included the top 11, 13, and 15 levels, respectively, as listed in Section 2, were conducted. The spectra and the Hovmöller diagrams shown in Fig. 6a–c and Fig. 6d–f, respectively, demonstrate that the thicker model ocean simulated a stronger MJO with a frequency closer to the observation and an eastward propagation similar to that in C–30NS and observations. In addition, the lead–lag relationship between precipitation (wind) and SST was more realistically simulated with increasing thickness (Fig. 6g–i).

This result suggests that the thickness of the upper ocean that interacts with the atmosphere strongly affects the frequency of the simulated MJO. A thinner (thicker) oceanic mixed layer is more quickly (slowly) recharged and discharged through heat exchange between the atmosphere and ocean and therefore likely fluctuates at a faster (slower) tempo. The simulated periodicity is therefore affected by the thickness of oceanic mixed layer (or heat content). Although this study suggests 60 m is an appropriate thickness to realistically simulate the periodicity of the MJO, we did not intend to suggest the exact thickness required for a proper simulation because it might depend on the model. The oceanic mixed layer should be adequately thick to contain a certain amount of heat to generate periodicity that is close to that observed. However,

https://doi.org/10.5194/gmd-2021-346
Preprint. Discussion started: 22 November 2021

Geoscientific Model Development Discussions

the reason for the intraseasonal time scale (i.e., 20-100 days) should be determined in future studies. This finding does not suggest a constant periodicity because periodicity might be affected by the time-varying structure of the atmosphere and ocean in the real world.

**4.4 Effects of coupling domains**

The MJO is a planetary-scale phenomenon. Given its large-scale circulation, the air–sea interaction affecting the MJO likely occurs in a much larger area than the region near the major convection anomalies. In this section, we discuss whether and how the coupling domain affects a model's ability to simulate the MJO. Four experiments considering the coupling in various domains (C–0_30N, C–0_30S, C–30_180E, and C–30E_75W) were conducted to investigate the effect of the coupling domain on the eastward propagation speed and periodicity of the MJO in the simulation. The results are shown in Fig. 7. The domains of the four experiments are shown in Fig. 1. The C–0_30N that considered the coupling in the tropics between the equator and 30°N simulated the least realistic MJO propagation in terms of W–FS (Fig. 7a), zonal wind–precipitation coupling (Fig. 7e), and SST–precipitation (Fig. 7i) of the four regional coupling experiments. By contrast, coupling only the tropics between the equator and 30°S simulated a more realistic MJO in all three aspects (i.e., spectrum in Fig. 7b, temporal evolution of precipitation/wind, and precipitation/SST coupling in Fig. 7f and 7j). Figure. 8a indicates that the positive precipitation anomalies simulated in C–0_30N stayed mainly north of the equator and did not shift southward in the MC as observed and in C–30NS, and the convection over the IO was unrealistically weak. By contrast, the southward detouring in the MC was realistically simulated in C–0_30S that coupled only the tropical ocean between the equator and 30°S. This result indicates that air–sea coupling occurring south of the equator is the

https://doi.org/10.5194/gmd-2021-346
Preprint. Discussion started: 22 November 2021



key to producing appropriate eastward propagation of the MJO through the MC. Without this coupling, the C–0_30N experiment failed to realistically simulate the eastward propagation of the MJO. This contrast can be attributed to the observed warmer ocean surface and higher moisture content found south of the equator in boreal winter, which comprise a more favorable environmental condition for air–sea coupling and convection–circulation coupling and the occurrence of the MJO.

MJO simulations can be affected by air–sea coupling in the longitudinal domain. Tseng et al. (2014) examined this effect by allowing coupling in different regions (e.g., the IO, WP, and IO + WP) and found that the IO + WP coupling experiment yielded the most satisfactory MJO simulation in terms of the zonal W–FS and eastward propagation characteristics. In this study, we conducted sensitivity experiments in which we allowed coupling in the tropics in two longitudinal domains, namely 30°E–180°E (C–30_180E) and 30°E–75°W (C–30E_75W). The 30°E–180°E region covered the IO and WP, and the 30°E–75°W region covered the IO and the entire tropical Pacific. As shown in Fig. 7, the C–30E_75W experiment simulated the MJO, yielding results more similar to the observation and those in C–30NS than to C–30_180E, with stronger eastward propagation and larger amplitudes in the spectrum (Fig. 7c and 7d) and Hovmöller diagrams of precipitation/wind (Fig. 7g and 7h) and precipitation/SST (Fig. 7k and 7l). The simulated MJO in C–30E_75W propagated further east than that in C–30_180E, particularly in Fig. 7k and 7l. The spatial distributions of circulation and precipitation shown in Fig. 8c and 8d indicated the presence of a stronger convective-coupled circulation system over the MC and WP in C–30E_75W. These results suggest that coupling over the entire tropical IO and Pacific could enhance the strength and eastward propagation of the MJO and encourage further propagation to the central Pacific.

https://doi.org/10.5194/gmd-2021-346
Preprint. Discussion started: 22 November 2021



### 4.5 Diurnal versus no diurnal cycle in air–sea coupling

The diurnal cycle in the MC can weaken the MJO and its eastward propagation (Hagos et al., 2016; Oh et al., 2013). We conducted an experiment to determine whether the daily mean value with the same coupling frequency would affect the MJO simulation. The coupling in the model was performed through heat flux exchange between the atmosphere and ocean. As mentioned in Section 2, air–sea fluxes were calculated twice for every time step (coupling 48 times per day, C–30NS) based on the instantaneous values of atmospheric and oceanic variables. In the experiment in which the diurnal cycle was removed (C–30NS–nD), air–sea fluxes were calculated as in C–30NS but were based on daily mean data. The results shown in Fig. 9 reveal the enhancement of the eastward-propagating signals in the MJO (e.g., a larger amplitude in spectrum; Fig. 9a) and further eastward and faster propagation (Fig. 9b) as well stronger coupling between precipitation and SST (Fig. 9c). The overall results are consistent with previous finding that the diurnal cycle tends to reduce the amplitude and propagation of the MJO, indicating that the weakening effect occurs through air–sea coupling in addition to those processes in the atmosphere. Previous studies have hypothesized that rapid interaction processes in the diurnal time scale tend to extract energy from the MJO, thus reducing both the strength and propagation tendency of the MJO. However, a comparison between the spectra of C–30NS and C–30NS–nD indicated that the experiment in which the diurnal cycle was removed appeared to oversimulate the MJO with unrealistic strength, suggesting that the effect of the diurnal cycle should be considered in the model to simulate a more realistic MJO. However, whether this is a common result in different models remain to be examined.

## 5 Discussion and conclusions

Air–sea coupling is a key mechanism for the successful simulation of the MJO

https://doi.org/10.5194/gmd-2021-346
Preprint. Discussion started: 22 November 2021




(Chang et al., 2019; DeMott et al., 2015; Jiang et al., 2015, 2020; Kim et al., 2010; Li et al., 2016; Li et al., 2020; Newman et al., 2009; Tseng et al., 2014). This study, following the study conducted by Tseng et al. (2014), demonstrated that coupling a high-resolution 1-D TKE ocean model (namely the SIT model) to the CAM5, namely the CAM5–SIT, significantly improved the MJO simulation over the standalone CAM5. The CAM5–SIT realistically simulated the MJO characteristics in many aspects (e.g., intraseasonal periodicity, eastward propagation, coherence in the low-frequency band, detouring propagation across the MC, tilting vertical structure, and intraseasonal variance in the WP).

Systematic sensitivity experiments were conducted to investigate the effects of the vertical resolution and the thickness of the 1-D ocean model, coupling domains, and the absence of the diurnal cycle. The results of all the sensitivity experiments are summarized in Fig. 10a and 10b, which show four common metrics for MJO evaluation. The four metrics are the propagation speed of the MJO (estimated from the U850 Hovmöller diagram) versus the power ratio of eastward- and westward-propagating 30–80-day signals (E/W ratio, derived from the zonal W–FS) in Fig. 10a and the eastward propagation speed of the 30–80-day filtered precipitation anomaly (estimated from the precipitation Hovmöller diagram) versus the variance explained by RMM1 and RMM2 (i.e., the sum of the variance explained by EOF1 and EOF2 based on Wheeler and Hendon, 2004) in Fig. 10b.

As for vertical resolution, we determined that the MJO simulation efficiency decreased when the vertical resolution of the SIT model was decreased from 1 m to 12 or 34 m, as observed in the C–LR12m and C–LR34m experiments, respectively. This finding, consistent with that reported by Tseng et al. (2014), suggests that a finer vertical resolution more effectively resolves temperature variations in the ocean warm layer and enhances atmospheric–ocean coupling, thus enabling the upper ocean to

https://doi.org/10.5194/gmd-2021-346
Preprint. Discussion started: 22 November 2021




more efficiently respond to atmospheric forcing by providing heat fluxes; this results in superior synchronization between the lower atmosphere and the upper ocean.

We observed that the thinner ocean mixed layer could speed up the eastward propagation of the MJO by producing more perturbations of shorter periodicity (Fig. 6) and resulted in a weaker MJO. The shallower oceanic mixed layer likely responded more quickly to atmospheric forcing but provided less heat fluxes to the atmosphere. Thus, the MJO propagated too fast with a weaker amplitude.

In the coupling domain sensitivity experiments, we investigated the essential coupling domain required to simulate the realistic MJO and the effect of the domain on the MJO simulation. Coupling only the northern tropics failed to simulate the eastward propagation, whereas coupling only the southern tropics yielded a more realistic MJO simulation, although this simulation was inferior to coupling the entire tropics. This contrast reveals the importance of the southern tropical ocean, especially in the MC where high SST and moisture content are noted. Coupling in the southern tropics is therefore essential for providing the energy required to maintain the MJO and its eastward propagation. By contrast, the northern tropics are relatively dry and cool. Coupling in this region is therefore less effective in improving MJO simulation.

In the longitudinal domain sensitivity experiments, we found that the MJO amplitude and the eastward extend of its eastward propagation were enhanced by extending the eastern boundary of the coupling domain from the tropical eastern IO to the tropical WP and further to the tropical eastern Pacific (Fig. 1). Further extension of the domain to cover the tropical Atlantic did not exhibit further enhancement (not shown). This result indicates that coupling in the tropical central and eastern Pacific, although not the major MJO signal regions (i.e., from the tropical IO to the tropical WP), still played a marked role in sustaining the MJO. We propose the following to explain this effect. Because of the planetary scale of the MJO, the near-surface

https://doi.org/10.5194/gmd-2021-346
Preprint. Discussion started: 22 November 2021




easterly circulation to the east of the convection core often extended to the tropical central and eastern Pacific where the climatological easterly prevailed. The coupling beyond the WP increased low-level moisture transport and convergence to the east of the convection and establish an environment suitable for the further eastward propagation of the MJO. This effect was likely terminated by the landmass of Central America when the tropical Atlantic was further included. Thus, a further eastward extension of the coupling domain exerted little effect on further enhancing the MJO. A diagnostic study on the effect of the longitudinal coupling domain is being conducted, and the results will be reported in a following paper.

The diurnal versus nondiurnal cycle experiment indicated that nondiurnal coupling tended to enhance eastward-propagating signals but slow the propagation. This result is consistent with the finding of previous studies that the diurnal cycle in the atmosphere extracts energy from the MJO, thus weakening it.

In this study, we demonstrated how air–sea coupling can improve the MJO simulation in a GCM. The findings are as follows.

(1) Better resolving the fine structure of the upper-ocean temperature and therefore the air–sea interaction led to more realistic intraseasonal variability in both SST and atmospheric circulation.

(2) An adequate thickness of the oceanic mixed layer is required to simulate a delayed response of the upper ocean to atmospheric forcing and lower-frequency fluctuation.

(3) Coupling the tropical eastern Pacific, in addition to the tropical IO and the tropical WP, can enhance the MJO and facilitate the further eastward propagation of the MJO to the dateline.

(4) Coupling the southern tropical ocean, instead of the norther tropical ocean, is essential for simulating a realistic MJO.

https://doi.org/10.5194/gmd-2021-346
Preprint. Discussion started: 22 November 2021



(5) Stronger MJO variability can be obtained without considering the diurnal cycle in coupling.

Our study confirmed the effectiveness of air–sea coupling for improving MJO simulation in a climate model and demonstrated how and where to couple. The findings enhance our understanding of the physical processes that shape the characteristics of the MJO.

*Code and data availability.* The model code of CAM5–SIT is available at https://doi.org/10.5281/zenodo.5510795. Input data of CAM5–SIT using the climatological Hadley Centre Sea Ice and Sea Surface Temperature dataset and GODAS data forcing, including 30-year numerical experiments, are available at https://doi.org/10.5281/zenodo.5510795.

*Author contributions.* HHH is the initiator and the primary investigator of the Taiwan Earth System Model project. YYL is the CAM5–SIT model developer and writes the majority part of the paper. WLT and LCJ assist in MJO analysis.

*Competing interests*. The authors declare that they have no conflict of interest.

*Acknowledgements.* The contribution from YYL, HHH, WLT, and LCJ to this study is supported by Ministry of Science and Technology of Taiwan under contracts MOST 110-2123-M-001-003, MOST 110-2811-M-001-603, MOST 109-2811-M-001-624 and MOST108-2811-M-001-643. We sincerely thank the National Center for Atmospheric Research and their Atmosphere Model Working Group (AMWG) for release CESM1.2.2. We thank the computational support from National Center for High530 performance Computing of Taiwan. This manuscript was edited by Wallace

Academic Editing.

## Reference

Adler, R. F., Huffman, G. J., Chang, A., Ferraro, R., Xie, P. P., Janowiak, J., Rudolf, B., Schneider, U., Curtis, S., Bolvin, D., Gruber, A., Susskind, J., Arkin, P. and Nelkini, E.: The Version 2.1 Global Precipitation Climatology Project (GPCP) Monthly Precipitation Analysis (1979 -Present), J. Hydrometeor., 4(6), 1147-1167, https://doi.org/10.1175/1525-7541(2003)004<1147:TVGPCP>2.0.CO;2, 2003.

Ahn, M.-S., Kim, D., Kang, D., Lee, J., Sperber, K. R., and Glecker, P. J., et al.: MJO propagation across the Maritime Continent: Are CMIP6 models better than CMIP5 models? Geophys. Res. Lett., 47, e2020GL087250. https://doi.org/10.1029/2020GL087250, 2020.

Ahn, M.-S., Kim, D., Sperber, K. R., Kang, I.-S., Maloney, E., Waliser, D., and Hendon, H.: MJO simulation in CMIP5 climate models: MJO skill metrics and process-oriented diagnosis, Clim. Dyn., 49, 4023–4045, https://doi.org/10.1007/s00382-017-3558-4, 2017.

Alappattu, D. P., Wang, Q., Kalogiros, J., Guy, N., and Jorgensen, D. P.: Variability of upper ocean thermohaline structure during a MJO event from DYNAMO aircraft observations, J. Geophys. Res. - Oceans, 122, 1122–1140, https://doi.org/10.1002/2016JC012137, 2017.

Amante, C., and Eakins, B. W.: ETOPO1 1 arc-minute globe relief model: Procedures, data sources and analysis, NOAA Tech. Memo. NESDIS NGDC-24, 19 pp., NOAA, Silver Spring, Md., 2009.

Behringer, D. W., and Xue, Y.: Evaluation of the global ocean data assimilation system at NCEP: The Pacific Ocean. Eighth Symposium on Integrated Observing and Assimilation Systems for Atmosphere, Oceans, and Land Surface, AMS 84th Annual Meeting, Washington State Convention and Trade Center, Seattle, Washington, 11-15. Derber, J.C., and A. Rosati, 1989: A global oceanic data assimilation system, J. Phys. Oceanogr., 19, 1333–1347, https://ams.confex.com/ams/pdfpapers/70720.pdf, 2004.

Bentsen, M., Bethke, I., Debernard, J. B., Iversen, T., Kirkevåg, A., Seland, Ø., Drange, H., Roelandt, C., Seierstad, I. A., Hoose, C., and Kristjánsson, J. E.: The Norwegian Earth System Model, NorESM1-M – Part 1: Description and basic evaluation of the physical climate, Geosci. Model Dev., 6, 687-720, https://doi.org/10.5194/gmd-6-687-2013, 2013.

Bernie, D, Guilyardi, E., Madec, G., Slingo, J., Woolnough, S., and Cole, J.: Impact of resolving the diurnal cycle in an ocean–atmosphere GCM. Part 2: a diurnally coupled CGCM, Clim.

https://doi.org/10.5194/gmd-2021-346
Preprint. Discussion started: 22 November 2021


Geoscientific Model Development
Discussions

Dynam., 31, 909–925, https://doi.org/10.1007/s00382-008-0429-z, 2008.

Boyle, J. S., Klein, S. A., Lucas, D. D., Ma, H.-Y., Tannahill, J., and Xie, S.: The parametric sensitivity of CAM5's MJO, J. Geophys. Res.-Atmos., 120, 1424–1444, https://doi.org/10.1002/2014JD022507, 2015.

Bui, H. X., and Maloney, E. D.: Changes in Madden-Julian Oscillation precipitation and wind variance under global warming, Geophys. Res. Lett., 45, 7148–7155, https://doi.org/10.1029/2018GL078504, 2018.

Chang, M.-Y., Li, T., Lin, P.-L., and Chang, T.-H.: Forecasts of MJO Events during DYNAMO with a Coupled Atmosphere-Ocean Model: Sensitivity to Cumulus Parameterization Scheme, J. Meteorol. Res., 33, 1016–1030, https://doi.org/10.1007/s13351-019-9062-5, 2019.

CLIVAR MADDEN–JULIAN OSCILLATION WORKING GROUP: MJO simulation diagnostics, J. Climate, 22, 3006-3030, https://doi.org/10.1175/2008JCLI2731.1, 2009.

Crueger, T., Stevens, B., and Brokopf, R.: The Madden–Julian Oscillation in ECHAM6 and the introduction of an objective MJO metric, J. Climate, 26, 3241–3257, https://doi.org/10.1175/JCLI-D-12-00413.1, 2013.

Danabasoglu, G., Lamarque, J. - F., Bacmeister, J., Bailey, D. A., DuVivier, A. K., and Edwards, J., et al.: The Community Earth System Model Version 2 (CESM2), J. Adv. Model. Earth Syst., 12, e2019MS001916, https://doi.org/10.1029/2019MS001916, 2020.

Dee, D. P., Uppala, S. M., Simmons, A. J., Berrisford, P., Poli, P., Kobayashi, S., Andrae, U., Balmaseda, M. A., Balsamo, G., Bauer, P., Bechtold, P., Beljaars, A. C. M., van de Berg, L., Bidlot, J., Bormann, N., Delsol, C., Dragani, R., Fuentes, M., Geer, A. J., Haimberger, L., Healy, S. B., Hersbach, H., Hólm, E. V., Isaksen, L., Kållberg, P., Köhler, M., Matricardi, M., McNally, A. P., Monge-Sanz, B. M., Morcrette, J.-J., Park, B.-K., Peubey, C., de Rosnay, P., Tavolato, C., Thépaut, J.-N. and Vitart, F.: The ERA-Interim reanalysis: configuration and performance of the data assimilation system, Q. J. R. Meteorol. Soc., 137: 553–597, https://doi.org/10.1002/qj.828, 2011.

de Szoeke, S. P., Skyllingstad, E. D., Zuidema, P., and Chandra, A. S.: Cold pools and their influence on the tropical marine boundary layer, J. Atmos. Sci., 74, 1149– 1168. https://doi.org/10.1175/JAS-D-16-0264.1, 2017.

DeMott, C. A., Klingaman, N. P., and Woolnough, S. J.: Atmosphere-ocean coupled processes in the Madden-Julian oscillation, Rev. Geophys., 53, 1099–1154, https://doi.org/10.1002/2014RG000478,

https://doi.org/10.5194/gmd-2021-346
Preprint. Discussion started: 22 November 2021

Geoscientific Model Development Discussions

2015.

DeMott, C. A., Klingaman, N. P., Tseng, W.-L., Burt, M. A., Gao, Y., and Randall, D. A.: The convection connection: How ocean feedbacks affect tropical mean moisture and MJO propagation, J. Geophys. Res.-Atmos., 124, 11,910–11,931, https://doi.org/10.1029/2019JD031015, 2019.

Gaspar, P., Gregoris, Y., and Lefevre, J.-M.: A simple eddy kinetic energy model for simulations of the oceanic vertical mixing: tests at station papa and long-term upper ocean study site, J. Geophys. Res. -Oceans, 95, 16179–16193, https://doi.org/10.1029/JC095iC09p16179, 1990.

Gonzalez, A. O., and Jiang, X.: Winter mean lower tropospheric moisture over the Maritime Continent as a climate model diagnostic metric for the propagation of the Madden-Julian oscillation, Geophys. Res. Lett., 44, https://doi.org/10.1002/2016GL072430, 2017.

Grassl, H.: The dependence of the measured cool skin of the ocean on wind stress and total heat flux, Bounday-Layer Meteorol., 10, 465-474, https://doi.org/10.1007/BF00225865, 1976.

Hannah, W. M., and Maloney, E. D.: The moist static energy budget in NCAR CAM5 hindcasts during DYNAMO, J. Adv. Model. Earth Syst., 6, 420–440, https://doi.org/10.1002/2013MS000272, 2014.

Hasse, L.: The sea surface temperature deviation and the heat flow at the sea–air interface, Bounday-Layer Meteorol., 1, 368-379, https://doi.org/10.1007/BF02186037, 1971.

Hagos, S. M., Zhang, C., Feng, Z., Burleyson, C. D., Mott, C. De, Kerns, B., Benedict, J. J., and Martini, M. N.: The impact of the diurnal cycle on the propagation of Madden-Julian Oscillation convection across the Maritime Continent, J. Adv. Model. Earth Syst., 8, 1552–1564, https://doi.org/10.1002/2016MS000725, 2016.

Heath, A., Gonzalez, A. O., Gehne, M., and Jaramillo, A.: Interactions of large-scale dynamics and Madden-Julian Oscillation propagation in multi-model simulations, J. Geophys. Res.-Atmos., 126, e2020JD033988. https://doi.org/10.1029/2020JD033988, 2021.

Hong, X., Reynolds, C. A., Doyle, J. D., May, P., and O'Neill, L.: Assessment of upper-ocean variability and the Madden-Julian Oscillation in extended-range air–ocean coupled mesoscale simulations, Dyn. Atmos. Oceans, 78, 89–105. https://doi.org/10.1016/j.dynatmoce.2017.03.002, 2017.

Hung, M.-P., Lin, J.-L., Wang, W., Kim, D., Shinoda, T., and Weaver, S. J.: MJO and convectively coupled equatorial waves simulated by CMIP5 climate models, J. Climate, 26, 6185–6214, https://doi.org/10.1175/JCLI-D-12-00541.1, 2013.

https://doi.org/10.5194/gmd-2021-346
Preprint. Discussion started: 22 November 2021

Geoscientific Model Development Discussions

Hurrell, J. W., Holland, M. M., Gent, P. R., Ghan, S., Kay, J. E., Kushner, P. J., Lamarque, J.-F., Large, W. G., Lawrence, D., Lindsay, K., Lipscomb, W. H., Long, M. C., Mahowald, N., Marsh, D. R., Neale, R. B., Rasch, P., Vavrus, S., Vertenstein, M., Bader, D., Collins, W. D., Hack, J. J., Kiehl, J., and Marshall, S.: The community Earth system model: A framework for collaborative research, B. Am. Meteorol. Soc., 94, 1319–1360, https://doi.org/10.1175/BAMS-D-12-00121, 2013.

Jiang, X., et al.: Vertical structure and physical processes of the MaddenJulian oscillation: Exploring key model physics in climate simulations, J. Geophys. Res.-Atmos., 120, 4718–4748, https://doi.org/10.1002/2014JD022375, 2015.

Jiang, X., Adames, Á. F., Kim, D., Maloney, E. D., Lin, H., and Kim, H., et al.: Fifty years of research on the Madden-Julian Oscillation: Recent progress, challenges, and perspectives, J. Geophys. Res.-Atmos., 125, e2019JD030911, https://doi.org/10.1029/2019JD030911, 2020.

Johnson, R. H., and Ciesielski, P. E.: Multiscale variability of the atmospheric boundary layer during DYNAMO, J. Atmos. Sci., 74, 4003–4021, https://doi.org/10.1175/JAS-D-17-0182.1, 2017.

Kaylor, R. E.: Filtering and decimation of digital time series, Tech. Rep. Note BN 850, Institute for Physical Science and Technology, University of Maryland at College Park, 14 pp, 1997.

Kim, D., Sobel, A. H., Maloney, E. D., Frierson, D. M. and Kang, I.-S.: A systematic relationship between intraseasonal variability and mean state bias in AGCM simulations, J. Climate, 24, 5506–5520. https://doi.org/10.1175/2011JCLI4177.1, 2011.

Kim, D., Kim H., and Lee M.-I.: Why does the MJO detour the Maritime Continent during austral summer? Geophys. Res. Lett., 44, 2579–2587, https://doi.org/10.1002/2017GL072643, 2017.

Kim, H.-M., Hoyos, C. D. and Webster, P. J. et al.: Ocean–atmosphere coupling and the boreal winter MJO, Clim Dynam., 35, 771–784, https://doi.org/10.1007/s00382-009-0612-x, 2010.

Kiranmayi, L., and Maloney, E. D.: Intraseasonal moist static energy budget in reanalysis data, J. Geophys. Res., 116, D21117, https://doi.org/10.1029/2011JD016031, 2011.

Lan, Y.-Y., Tsuang, B.-J., Tu, C.-Y., Wu, T.-Y., Chen, Y.-L., and Hsieh, C.-I.: Observation and Simulation of Meteorology and Surface Energy Components over the South China Sea in Summers of 2004 and 2006, Terr. Atmos. Ocean. Sci., 21, 325-342, https://doi.org/ 10.3319/TAO.2009.04.07.01(A), 2010.

Lee, H.-T., and NOAA CDR Program: NOAA Climate Data Record (CDR) of Daily Outgoing Longwave Radiation (OLR), Version 1.2,

https://doi.org/10.5194/gmd-2021-346
Preprint. Discussion started: 22 November 2021




NOAA National Climatic Data Center, https://doi.org/10.7289/V5SJ1HH2, 2011.

Li, T., Ling, J., and Hsu, P.-C.: Madden–Julian Oscillation: Its discovery, dynamics, and impact on East Asia, J. Meteor. Res., 34, 20–42, https://doi.org/10.1007/s13351-020-9153-3, 2020.

Li, T., Tam, F., Fu, X., Zhou, T., and Zhu, W.: Causes of the intraseasonal SST variability in the tropical Indian Ocean, Atmos. Oceanic Sci. Lett., 1, 18–23, https://doi.org/10.1080/16742834.2008.11446758, 2008.

Li, X., Tang, Y., Zhou, L., Chen, D. and Yao, Z.: Assessment of Madden–Julian oscillation simulations with various configurations of CESM, Clim. Dynam., 47, 2667–2690, https://doi.org/10.1007/s00382-016-2991-0, 2016.

Ling, J., Zhao, Y. and Chen, G.: Barrier effect on MJO propagation by the Maritime Continent in the MJO Task Force/GEWEX atmospheric system study models, J. Climate, 32, 5529–5547, https://doi.org/10.1175/JCLI-D-18-0870.1, 2019.

Madden, R. A., and Julian, P. R.: Description of global-scale circulation cells in the tropics with a 40-50 day period, J. Atmos. Sci., 29, 1109-1123, https://doi.org/10.1175/1520-0469(1972)029<1109:DOGSCC>2.0.CO;2, 1972.

Madden, R. A., and Julian, P. R.: Observations of the 40-50 day tropical oscillation - A review, Mon. Weather Rev., 122, 814– 837, https://doi.org/10.1175/1520-0493(1994)122<0814:OOTDTO>2.0.CO;2, 1994.

Mellor, G. L., and Yamada, T.: Development of a turbulence closure model for geophysical fluid problems, Rev. Geophys., 20, 851-875, https://doi.org/10.1029/RG020i004p00851, 1982.

Neale, R. B., et al.,: Description of the NCAR Community Atmosphere Model (CAM 5.0), NCAR Tech. Note NCAR/TN-486+STR, 289 pp., Natl. Cent. for Atmos. Res, Boulder, Colo., 2012.

Newman, M., Sardeshmukh, P. D., and Penland, C.: How important is air–sea coupling in ENSO and MJO evolution? J. Clim., 22, 2958– 2977, https://doi.org/10.1175/2008JCLI2659.1, 2009.

Oh, J., Kim, B., and Kim, K. et al.: The impact of the diurnal cycle on the MJO over the Maritime Continent: a modeling study assimilating TRMM rain rate into global analysis, Clim. Dynam., 40, 893–911, https://doi.org/10.1007/s00382-012-1419-8, 2013.

Paulson, C. A. and Simpson, J. J.: The temperature difference across the cool skin of the ocean, J. Geophys. Res., 86, 11044-11054, https://doi.org/10.1029/JC086iC11p11044, 1981.

https://doi.org/10.5194/gmd-2021-346
Preprint. Discussion started: 22 November 2021



Pei, S., Shinoda, T., Soloviev, A., and Lien, R.-C.: Upper ocean response to the atmospheric cold pools associated with the Madden-Julian Oscillation, Geophys. Res. Lett., 45, 5020–5029, https://doi.org/10.1029/2018GL077825, 2018.

Pujiana, K., Moum, J. N., and Smyth, W. D.: The role of subsurface turbulence in redistributing upper-ocean heat, freshwater, and momentum in response to the MJO in the equatorial Indian Ocean, J. Phys. Oceanogr., 48, 197–220, https://doi.org/10.1175/JPO-D-17-0146.1, 2018.

Rayner, N. A., Parker, D. E., Horton, E. B., Folland, C. K., Alexander, L. V., Rowell, D. P., Kent, E. C., and Kaplan, A.: Global analyses of sea surface temperature, sea ice, and night marine air temperature since the late nineteenth century, J. Geophys. Res., 108(D14), 4407, https://doi.org/10.1029/2002JD002670, 2003.

Ren, P. F., Gao, L., and Ren, H.-L. et al.: Representation of the Madden–Julian Oscillation in CAMSCSM, J. Meteor. Res., 33, 627–650, https://doi.org/10.1007/s13351-019-8118-x, 2019.

Reynolds R. W., and Smith T. M.: A high-resolution global sea surface temperature climatology, J. Clim., 8(6),1571–1583, https://doi.org/10.1175/1520-0442(1995)008<1571:AHRGSS>2.0.CO;2, 1995.

Schreck, C. J., Lee, H.-T., and Knapp, K. R.: HIRS outgoing longwave radiation—Daily climate data record: Application toward identifying tropical subseasonal variability, Remote Sens., 10, 1325. https://doi.org/10.3390/rs10091325, 2018.

Sobel, A. H., Maloney, E. D., Bellon, G., and Dargan, M. F.: The role of surface heat fluxes in tropical intraseasonal oscillations, Nat. Geosci., 1, 653–657, https://doi.org/10.1038/ngeo312, 2008.

Subramanian, A. C., Jochum, M., Miller, A. J., Murtugudde, R., Neale, R. B., and Waliser, D. E.: The Madden–Julian oscillation in CCSM4, J. Climate, 24, 6261–6282, https://doi.org/10.1175/JCLI-D-11-00031.1, 2011.

Tseng, W.-L., Tsuang, B.-J., Keenlyside, N. S., Hsu, H.-H. and Tu, C.-Y.: Resolving the upper-ocean warm layer improves the simulation of the Madden-Julian oscillation, Clim. Dynam., 44, 1487–1503, https://doi.org/10.1007/s00382-014-2315-1, 2014.

Tseng, W.-L., Hsu, H.-H., Keenlyside, N., Chang, C.-W. J., Tsuang, B.-J., Tu, C.-Y., and Jiang, L.-C.: Effects of Orography and Land–Sea Contrast on the Madden–Julian Oscillation in the Maritime Continent: A Numerical Study Using ECHAM-SIT, J. Climate, 30, 9725-9741, https://doi.org/10.1175/JCLI-D-17-0051.1, 2017.

Tu, C.-Y., and Tsuang, B.-J.: Cool-skin simulation by a one-column ocean model, Geophys. Res. Lett., 32, L22602, https://doi.org/10.1029/2005GL024252, 2005.

https://doi.org/10.5194/gmd-2021-346
Preprint. Discussion started: 22 November 2021

Geoscientific Model Development Discussions
Open Access EGU

Wang, W., Hung, M.-P., Weaver, S. J., Kumar, A., and Fu, X.: MJO prediction in the NCEP Climate Forecast System version 2, Clim. Dyn., 42, 2509–2520, https://doi.org/10.1007/s00382-013-1806-9, 2014.

Wheeler, M. C, and Hendon, H. H.: An all-season real-time multivariate MJO index: development of an index for monitoring and prediction, Mon. Weather Rev., 132, 1917–1932, https://doi.org/10.1175/1520-0493(2004)132<1917:AARMMI>2.0.CO;2, 2004.

Wheeler, M., and Kiladis, G. N.: Convectively coupled equatorial waves: Analysis of clouds and temperature in the wavenumber-frequency domain, J. Atmos. Sci., 56, 374– 399, https://doi.org/10.1175/1520-0469(1999)056<0374:CCEWAO>2.0.CO;2, 1999.

Woolnough, S. J., Vitard, F., and Balmaseda, M. A.: The role of the ocean in the Madden–Julian oscillation: Implications for MJO prediction, Quart. J. Roy. Meteor. Soc., 133, 117–128, https://doi.org/10.1002/qj.4, 2007.

Wu, J.: On the cool skin of the ocean, Bounday-Layer Meteorol., 31, 203-207, https://doi.org/10.1007/BF00121179, 1985.

Wu, C.-H., and Hsu, H.-H.: Potential Influence of Topography on the MJO in the Maritime Continent, J. Climate, 22, 5433-5448, https://doi.org/10.1175/2009JCLI2825.1, 2009.

Yoneyama, K., Zhang, C., and Long, C.: Tracking pulses of the Madden–Julian oscillation, Bull. Amer. Meteor. Soc., 94, 1871–1891, https://doi.org/10.1175/BAMS-D-12-00157.1, 2013.

Zhang, C.: Madden-Julian oscillation, Rev. Geophys., 43, RG2003, https://doi.org/10.1029/2004RG000158, 2005.

Zhang, C., and Yoneyama, K.: CINDY/DYNAMO field campaign: Advancing our understanding of MJO initiation. The Global Monsoon System, C.-P. Chang et al., Eds., World Scientific Series on Asia-Pacific Weather and Climate, Vol. 9, World Scientific Publishing Co., 339–348, https://doi.org/10.1142/9789813200913_0027, 2017.

https://doi.org/10.5194/gmd-2021-346
Preprint. Discussion started: 22 November 2021

Geoscientific Model Development Discussions
Open Access

**Table 1.** List of experiments

| Section | Category | Experiments | Description |
|---|---|---|---|
| 4.1 | Coupled or uncoupled | A–CTL | Standalone CAM5.3 forced by observed SST climatology |
| | | C–30NS | CAM5.3 coupled with SIT over the tropical domain (30°S–30°N), with finest vertical resolution (up to submarine topography) and diurnal cycle; the frequency of CAM5 being exchanged with CPL is 48 times per day |
| 4.2 | Upper-ocean vertical resolution | C–LR12m | The first ocean vertical level starts at 11.8 m (beside SST and cool skin layer) |
| | | C–LR34m | The first ocean vertical level starts at 34.2 m (beside SST and cool skin layer) |
| 4.3 | Lowest boundary of SIT | C–HR1mB10m | The lowest boundary of SIT has a depth of 10 m (middle grid) |
| | | C–HR1mB30m | The lowest boundary of SIT has a depth of 30 m (middle grid) |
| | | C–HR1mB60m | The lowest boundary of SIT has a depth of 60 m (middle grid) |
| 4.4 | Regional coupling domain in latitude | C–0_30N | Coupled in the tropical northern hemisphere (0°N–30°N, 0°E–360°E) |
| | | C–0_30S | Coupled in the tropical southern hemisphere (0°S–30°S, 0°E–360°E) |
| | Regional coupling domain in longitude | C–30_180E | Coupled in the Indo-Pacific (30°S–30°N, 30°E–180°E) |
| | | C–30E_75W | Coupled over the Indian Ocean and Pacific Ocean (30°S–30°N, 30°E–75°W) |
| 4.5 | Absence of the diurnal cycle | C–30NS–nD | Absence of the diurnal cycle in C–30NS; the CAM5.3 daily atmospheric mean of surface wind, temperature, total precipitation, net surface heat flux u-stress and v-stress over water trigger the SIT and daily mean SST feedback to atmosphere; the frequency of CAM5 is exchanged with CPL 48 times per day |

The CAM5.3 AGCM is used in all experiments
Experiment abbreviations: “A” means standalone AGCM simulation. “C” means the CAM5.3 coupled to the SIT model.

https://doi.org/10.5194/gmd-2021-346
Preprint. Discussion started: 22 November 2021



**Figure List**

**Figure 1.** Schematics of coupled and uncoupled domains in the regional coupling experiment: (a) C–30NS, (b) C–0_30N, (c) C–0_30S, (d) C–30_180E, and (e) C–30E_75W. The background is the climatological mean SST in December–February (DJF).

**Figure 2.** (a)–(c) Zonal wavenumber–frequency spectra for 850-hPa zonal wind averaged over 10°S–10°N in boreal winter after removing the climatological mean seasonal cycle. Vertical dashed lines represent periods at 80 and 30 days, respectively. (d)–(f) Hovmöller diagrams of the correlation between the precipitation averaged over 10°S–5°N, 75–100°E and the intraseasonally filtered precipitation (color) and 850-hPa zonal wind (contour) averaged over 10°N–10°S. (g)–(i) Zonal wavenumber–frequency power spectra of anomalous OLR (colors) and phase lag with U850 (vectors) for the symmetric component of tropical waves, with the vertically upward vector representing a phase lag of 0° with phase lag increasing clockwise. Three dispersion straight lines with increasing slopes represent the equatorial Kelvin waves (derived from the shallow water equations) corresponding to three equivalent depths, 12, 25, and 50 m, respectively. (j)–(l) Composites of 20–100-day filtered OLR (W $m^{-2}$, shaded) and 850-hPa wind (m $s^{-1}$, *vector*) for MJO phase 5 when deep convection is the strongest over the MC and 850-hPa wind, with the reference vector (1 m $s^{-1}$) shown at the top right of each panel, and (m)–(o) 15°N–15°S averaged p-vertical velocity anomaly (Pa $s^{-1}$, shaded) and moist static energy anomaly (W $m^{-2}$, contour, interval 0.003); solid, dashed, and thick-black lines represent positive, negative, and zero values, respectively. The number of days used to generate the composite is shown at the bottom right corner of each panel. (a), (d), (g), (j), and (m) are from observations; (b), (e), (h), (k), and (n) are from the C–30NS; and (c), (f), (i), (l), and (o) are from the A–CTL.

**Figure 3.** Evolution of the filtered OLR anomaly (W $m^{-2}$, shaded) and 850-hPa wind (m $s^{-1}$, *vector*) at phase 2, 4, 6, and 8: (a) observation, (b) C–30NS, and (c) A–CTL. The unit of the reference vector shown at the top right corner of each panel is m $s^{-1}$, and the number of days used for the composite is shown at the bottom right corner of each panel.

**Figure 4.** (a)–(c) Phase-longitude Hovmöller diagrams of 20–100-day filtered precipitation (mm $day^{-1}$, shaded) and SST anomaly (K, contour) averaged over 10°N–10°S from phase 1 to 8. Contour interval is 0.03; solid, dashed, and thick-black lines represent positive, negative, and zero values, respectively. (d)–(f) Phase-vertical

https://doi.org/10.5194/gmd-2021-346
Preprint. Discussion started: 22 November 2021

Geoscientific Model Development
Discussions

Hovmöller diagrams of 20–100-day moisture divergence (shading, $10^{-6}$ g kg$^{-1}$ s$^{-1}$) and zonal wind (contoured, m s$^{-1}$) averaged over 10°N–10°S, 120–150°E; solid, dashed, and thick-black curves are positive, negative, and zero values, respectively. (g)–(i) Variation of 30–60-day filtered precipitation in the eastern IO and the WP in observation (color shading), and the ratio between intraseasonal and total variance (contoured) and (j)–(l) composites 20–100-day filtered SST (K, shaded) and 850-hPa winds (m s$^{-1}$, *vector*) at phase 7 when deep convection was the strongest over the dateline. Reference vector shown at the top right corner of each panel. (a), (d), (g), and (j) are from the observation; (b), (e), (h), and (k) are from the C–30NS; and (c), (f), (i), and (l) are from the A–CTL.

**Figure 5.** (a)–(b) Same as in Fig. 2(a) but for the C-LR12m and C-LR34m. (c)–(d) Same as in Fig. 2(d) but for the C-LR12m and C-LR34m. (e)–(f) Same as in Fig. 4(a) but for the C-LR12m and C-LR34m.

**Figure 6.** Same as in Fig. 5 but for the C–HR1mB10m, C–HR1mB30m, and C–HR1mB60m.

**Figure 7.** Same as in Fig. 5 but for the C–0_30N, C–0_30S, C–30_180E, and C–30E_75W.

**Figure 8.** Same as in Fig. 3 but for phase 5 in the C–0_30N, C–0_30S, C–30_180E, and C–30E_75W.

**Figure 9.** Similar as in Fig. 5 but for the C–30NS–nD.

**Figure 10.** Scattered plots of various MJO indices in observation and 12 experiments: (a) power ratio of east/west propagating waves of wavenumber 1–3 of 850-hPa zonal winds (X-axis) with a 30–80-day period and eastward propagation speed of U850 anomaly (Y-axis) from the Hovmöller diagram and (b) RMM1 and RMM2 variance and eastward propagation speed of the filtered precipitation anomaly derived from the Hovmöller diagram.

https://doi.org/10.5194/gmd-2021-346
Preprint. Discussion started: 22 November 2021



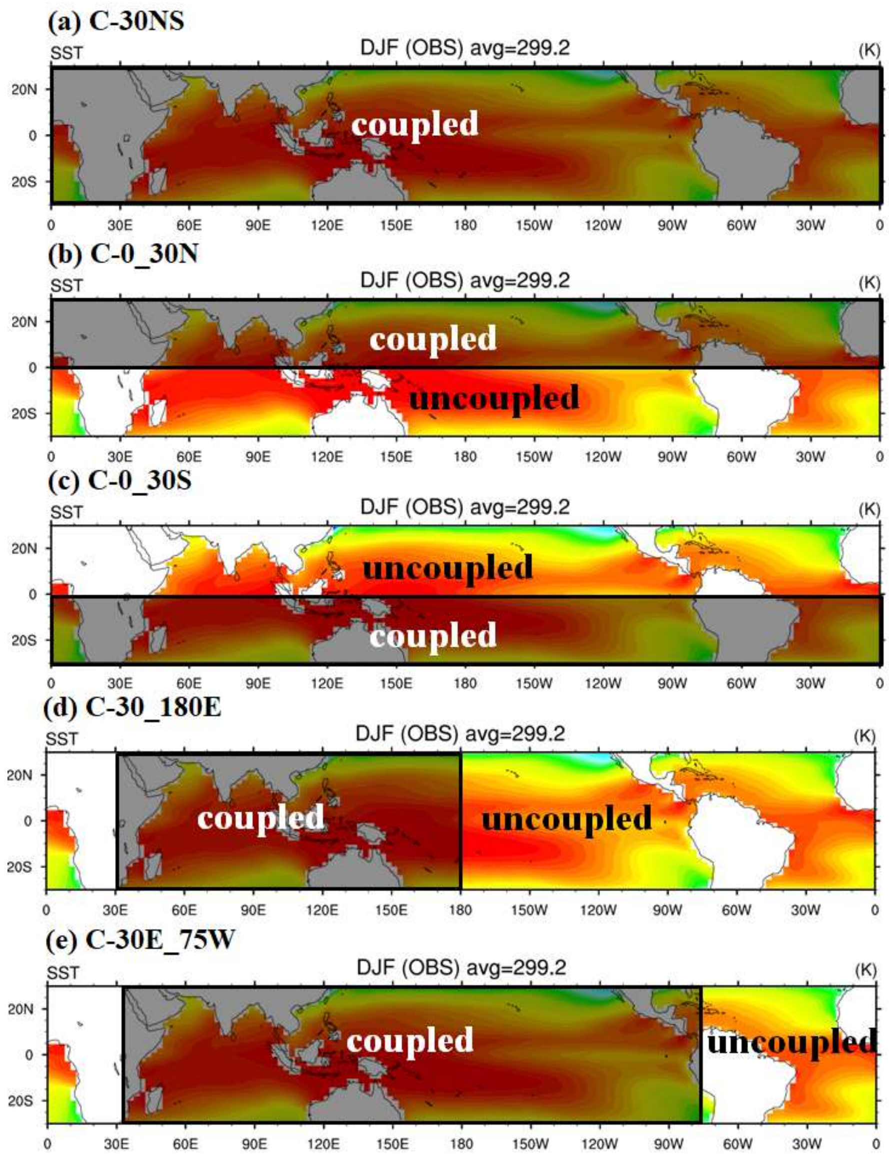


**Figure 1.** Schematics of coupled and uncoupled domains in the regional coupling experiment: (a) C–30NS, (b) C–0_30N, (c) C–0_30S, (d) C–30_180E, and (e) C–30E_75W. The background is the climatological mean SST in December–February (DJF).

https://doi.org/10.5194/gmd-2021-346
Preprint. Discussion started: 22 November 2021


Geoscientific Model Development
Discussions

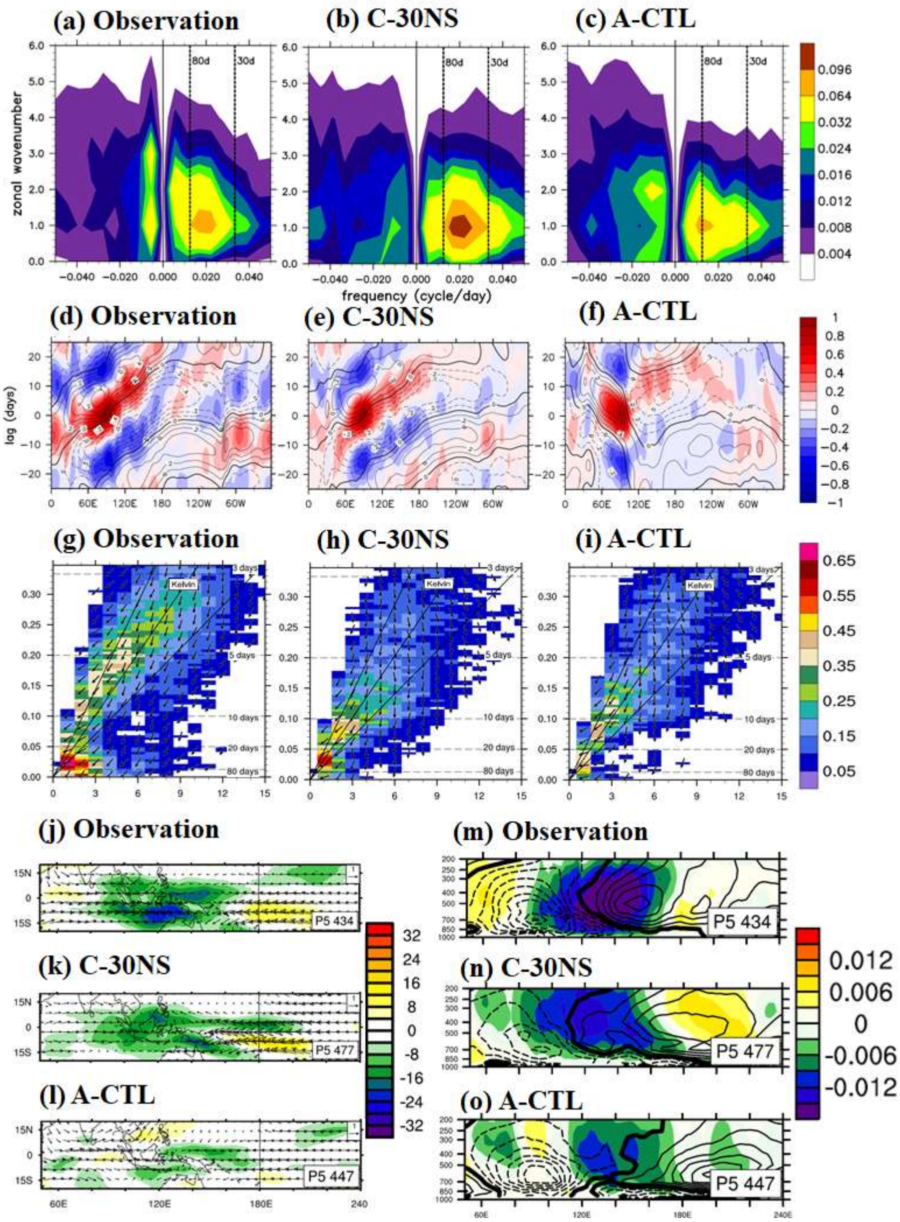


**Figure 2.** (a)–(c) Zonal wavenumber–frequency spectra for 850-hPa zonal wind averaged over 10°S–10°N in boreal winter after removing the climatological mean seasonal cycle. Vertical dashed lines represent periods at 80 and 30 days, respectively. (d)–(f) Hovmöller diagrams of the correlation between the precipitation averaged over 10°S–5°N, 75–100°E and the intraseasonally filtered precipitation (color) and 850-hPa zonal wind (contour) averaged over 10°N–10°S. (g)–(i) Zonal wavenumber–

https://doi.org/10.5194/gmd-2021-346
Preprint. Discussion started: 22 November 2021

Geoscientific Model Development
Discussions

frequency power spectra of anomalous OLR (colors) and phase lag with U850 (vectors) for the symmetric component of tropical waves, with the vertically upward vector representing a phase lag of 0° with phase lag increasing clockwise. Three dispersion straight lines with increasing slopes represent the equatorial Kelvin waves (derived from the shallow water equations) corresponding to three equivalent depths, 12, 25, and 50 m, respectively. (j)–(l) Composites of 20–100-day filtered OLR (W $m^{-2}$, shaded) and 850-hPa wind (m $s^{-1}$, *vector*) for MJO phase 5 when deep convection is the strongest over the MC and 850 hPa wind, with the reference vector (1 m $s^{-1}$) shown at the top right of each panel, and (m)–(o) 15°N–15°S averaged p-vertical velocity anomaly (Pa $s^{-1}$, shaded) and moist static energy anomaly (W $m^{-2}$, contour, interval 0.003); solid, dashed, and thick-black lines represent positive, negative, and zero values, respectively. The number of days used to generate the composite is shown at the bottom right corner of each panel. (a), (d), (g), (j), and (m) are from observations; (b), (e), (h), (k), and (n) are from the C–30NS; and (c), (f), (i), (l), and (o) are from the A–CTL.

https://doi.org/10.5194/gmd-2021-346
Preprint. Discussion started: 22 November 2021




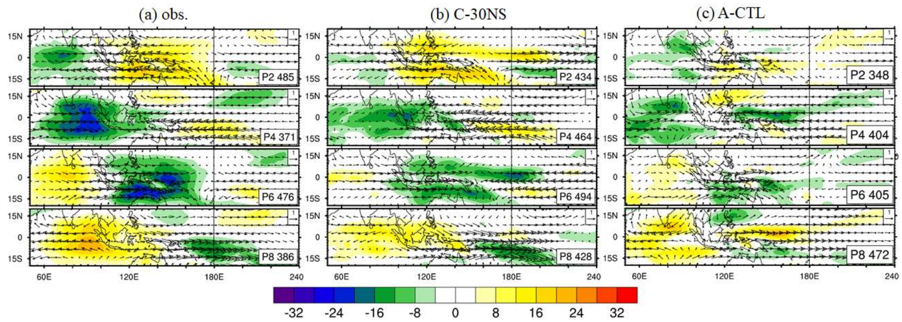


**Figure 3.** Evolution of the filtered OLR anomaly (W m$^{-2}$, shaded) and 850-hPa wind (m s$^{-1}$, *vector*) at phase 2, 4, 6, and 8: (a) observation, (b) C–30NS, and (c) A–CTL. The unit of the reference vector shown at the top right corner of each panel is m s$^{-1}$, and the number of days used for the composite is shown at the bottom right corner of each panel.

https://doi.org/10.5194/gmd-2021-346
Preprint. Discussion started: 22 November 2021


Geoscientific Model Development
Discussions

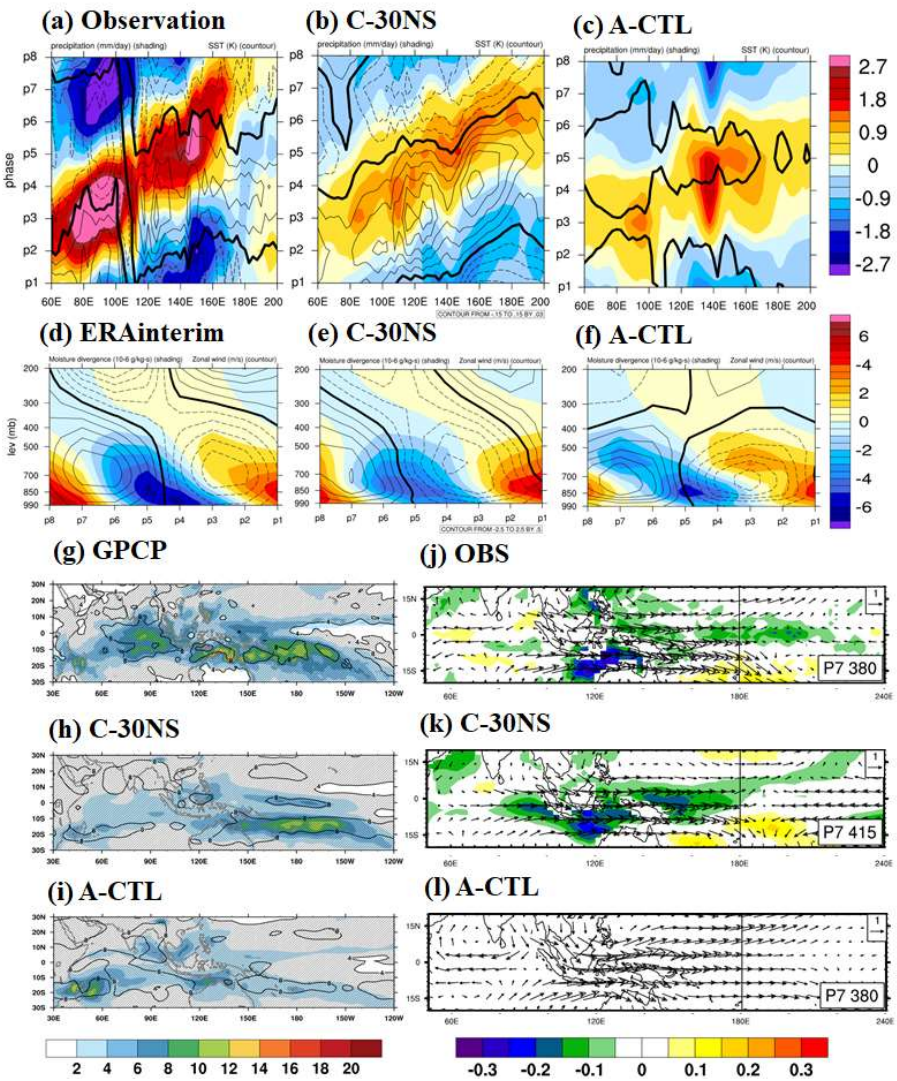


**Figure 4.** (a)–(c) Phase-longitude Hovmöller diagrams of 20–100-day filtered precipitation (mm day$^{-1}$, shaded) and SST anomaly (K, contour) averaged over 10°N–10°S from phase 1 to 8. Contour interval is 0.03; solid, dashed, and thick-black lines represent positive, negative, and zero values, respectively. (d)–(f) Phase-vertical Hovmöller diagrams of 20–100-day moisture divergence (shading, $10^{-6}$ g kg$^{-1}$ s$^{-1}$) and zonal wind (contoured, m s$^{-1}$) averaged over 10°N–10°S, 120–150°E; solid, dashed, and thick-black curves are positive, negative, and zero values, respectively. (g)–(i) Variation of 30–60-day filtered precipitation in the eastern IO and the WP in

https://doi.org/10.5194/gmd-2021-346
Preprint. Discussion started: 22 November 2021




observation (color shading), and the ratio between intraseasonal and total variance (contoured) and (j)–(l) composites 20–100-day filtered SST (K, shaded) and 850-hPa winds (m $s^{-1}$, *vector*) at phase 7 when deep convection was the strongest over the dateline. Reference vector shown at the top right corner of each panel. (a), (d), (g), and (j) are from the observation; (b), (e), (h), and (k) are from the C–30NS; and (c), (f), (i), and (l) are from the A–CTL.

https://doi.org/10.5194/gmd-2021-346
Preprint. Discussion started: 22 November 2021




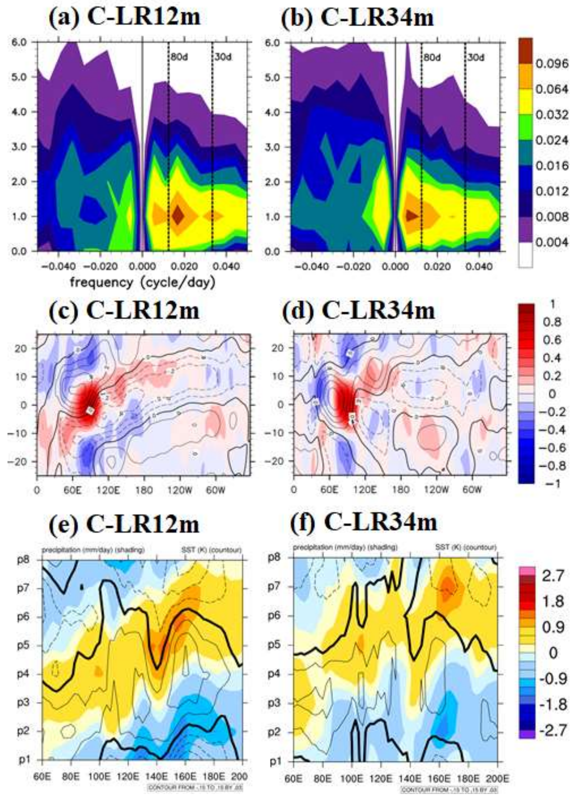


**Figure 5.** (a)–(b) Same as in Fig. 2(a) but for the C-LR12m and C-LR34m. (c)–(d) Same as in Fig. 2(d) but for the C-LR12m and C-LR34m. (e)–(f) Same as in Fig. 4(a) but for the C-LR12m and C-LR34m.

https://doi.org/10.5194/gmd-2021-346
Preprint. Discussion started: 22 November 2021

Geoscientific Model Development
Discussions
Open Access

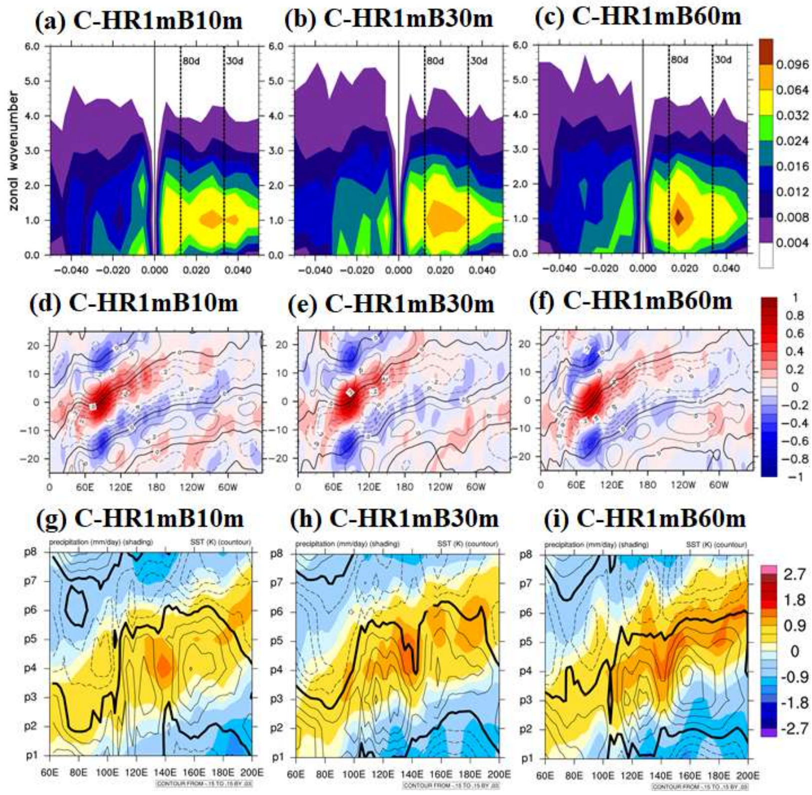


**Figure 6.** Same as in Fig. 5 but for the C–HR1mB10m, C–HR1mB30m, and C–HR1mB60m.

https://doi.org/10.5194/gmd-2021-346
Preprint. Discussion started: 22 November 2021




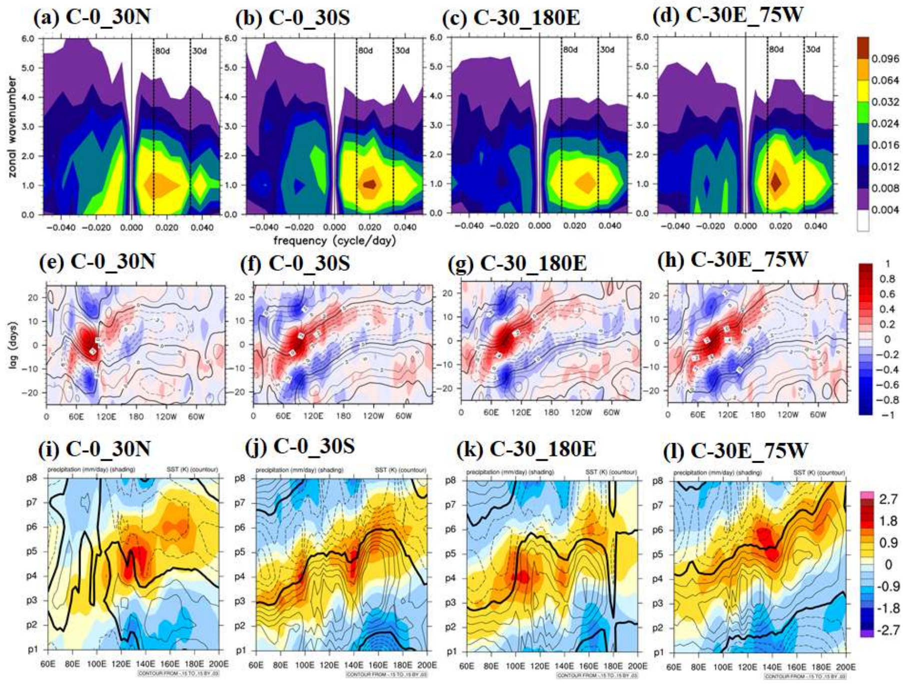


**Figure 7.** Same as in Fig. 5 but for the C–0_30N, C–0_30S, C–30_180E, and C–30E_75W.

https://doi.org/10.5194/gmd-2021-346
Preprint. Discussion started: 22 November 2021



1119 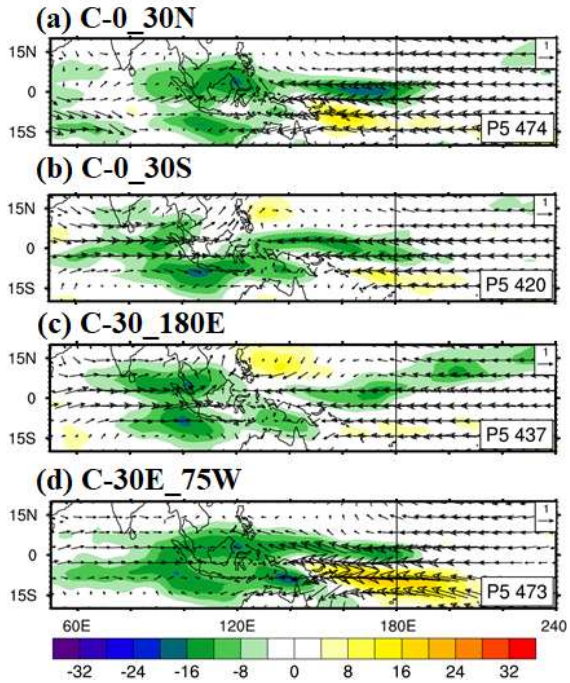


1121 **Figure 8.** Same as in Fig. 3 but for phase 5 in the C–0_30N, C–0_30S, C–30_180E,
1122 and C–30E_75W.

https://doi.org/10.5194/gmd-2021-346
Preprint. Discussion started: 22 November 2021



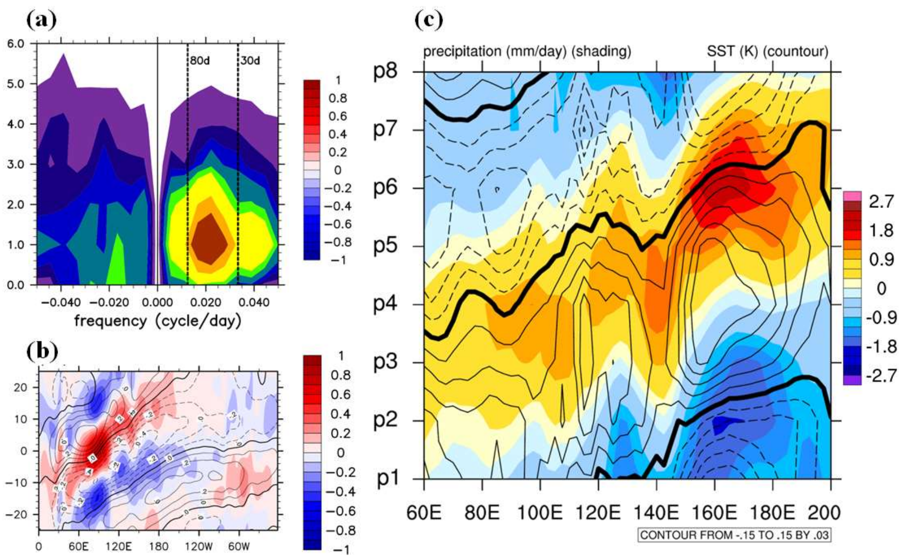


**Figure 9.** Similar as in Fig. 5 but for the C–30NS–nD.

https://doi.org/10.5194/gmd-2021-346
Preprint. Discussion started: 22 November 2021



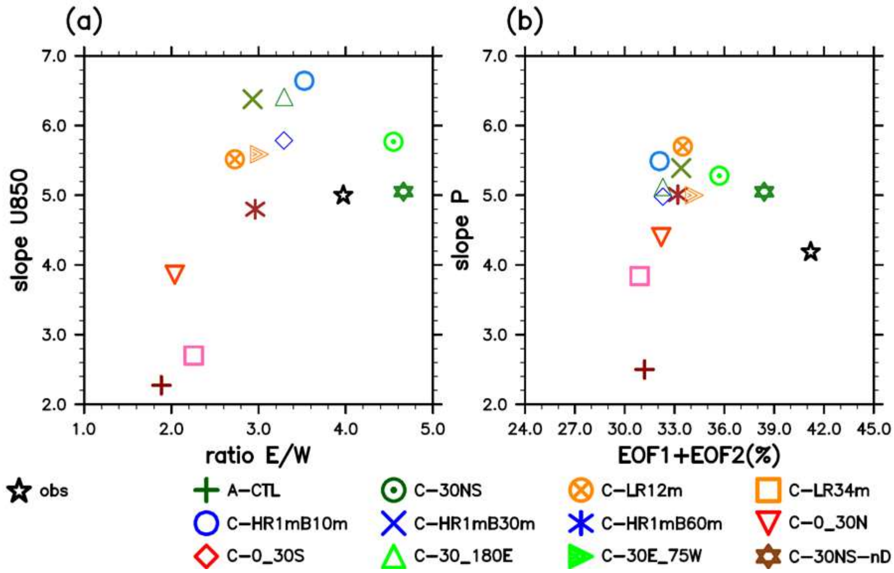


**Figure 10.** Scattered plots of various MJO indices in observation and 12 experiments: (a) power ratio of east/west propagating waves of wavenumber 1–3 of 850-hPa zonal winds (X-axis) with a 30–80-day period and eastward propagation speed of U850 anomaly (Y-axis) from the Hovmöller diagram and (b) RMM1 and RMM2 variance and eastward propagation speed of the filtered precipitation anomaly derived from the Hovmöller diagram.